frontiers | Frontiers in Materials

ORIGINAL RESEARCH
published: 24 May 2022
doi: 10.3389/fmats.2022.825120

Effect of Y Concentration on the *In Situ* Growth Behavior and Corrosion Protection of the MgAlY-LDH Sealing Film on the Anodized Surface of Mg–2Zn–4Y Alloy

Yuqi Hong[1,2], Liang Wu[1,2], Xinyi Zhang[1,2], Guoxiang Zhan[1,2], Yanning Chen[1,2], Wenhui Yao[1,2], Xu Dai[1,2], Tao Wu[1,2], Xiaowei Dai[1,2], Jianpeng Xiang[1,2], Yan Zhou[1,2] and Fusheng Pan[1,2]*

[1]State Key Laboratory of Mechanical Transmission, College of Materials Science and Engineering, Chongqing University, Chongqing, China, [2]National Engineering Research Center for Magnesium Alloys, Chongqing University, Chongqing, China

OPEN ACCESS

Edited by:
Daokui Xu,
Chinese Academy of Sciences (CAS), China

Reviewed by:
Xiaopeng Lu,
Northeastern University, China
You Zhang,
Beijing Institute of Petrochemical Technology, China

***Correspondence:**
Liang Wu
wuliang@cqu.edu.cn

Specialty section:
This article was submitted to Environmental Degradation of Materials, a section of the journal Frontiers in Materials

Received: 30 November 2021
Accepted: 20 April 2022
Published: 24 May 2022

Citation:
Hong Y, Wu L, Zhang X, Zhan G, Chen Y, Yao W, Dai X, Wu T, Dai X, Xiang J, Zhou Y and Pan F (2022) Effect of Y Concentration on the In Situ Growth Behavior and Corrosion Protection of the MgAlY-LDH Sealing Film on the Anodized Surface of Mg–2Zn–4Y Alloy. Front. Mater. 9:825120. doi: 10.3389/fmats.2022.825120

The successful doping of Yttrium (Y) in the Mg-Al layered double hydroxide film (MgAlY-LDHs) is obtained by hydrothermal way on the anodic oxide film of Mg-2Zn-4Y alloys. The composition, morphology and structure of MgAlY-LDHs were characterized by the Fourier transform infrared spectroscopy (FT-IR), X-ray diffractometer (XRD), field-emission scanning electronic microscope (FE-SEM) and energy dispersive spectrometry (EDS) respectively. The electrochemical behavior was observed by polarization curves and electrochemical impedance spectroscopy (EIS). Y ions can be incorporated into the MgAl-LDHs film in a completely isomorphic replacement manner and have the ability to improve the corrosion resistance of the film. Moreover, the ternary LDHs film grown in situ on the Mg-2Zn-4Y alloy provides a high possibility for the corrosion resistance of industrial metals. The schematic representation of electrochemical behavior and the growth mechanism of MgAlY-LDHs nanosheet are as following eventually.

Keywords: ion concentration, anode oxide film, yttrium, ternary-layered double hydroxides, corrosion resistance

1 INTRODUCTION

Magnesium alloys are considered to have a bright prospect because of their low density and environmentally friendly properties (Mordike and Ebert, 2001; Prado and Cepeda-Jiménez, 2015; Polmear, 2017). However, the high chemical activity of magnesium leads to its susceptibility to corrosion, limiting its industrial application (Srinivas et al., 2022). Therefore, the corrosion and protection of magnesium alloys have been listed as an important research topic in the material field in recent years. At present, the main method to effectively improve the corrosion resistance is the technology of surface coating, which is to prevent the corrosion of metal materials by a special treatment process and physical barrier method to limit the contact between the external corrosion medium and internal matrix (Stoltenhoff et al., 2002). Among the rest, anodic oxidation is the most effective method. Because of its simple and mature process, this method is widely used (Hornberger et al., 2012; Atrens, 2015). However, the magnesium alloy matrix is unprotected when the film is in the corrosive environment because of the porous and loose structure of the anodic oxide surface (Blawert et al., 2006). This is why magnesium anodization is rarely used commercially to improve

corrosion resistance (Blawert et al., 2006). Therefore, it is necessary to research an effective way to seal the anodic oxide film (Huang et al., 2014).

The layered double hydroxides (LDHs) have the possible ability to possess an active corrosion system. LDHs are a typical two-dimensional layered nanomaterial that has broad prospects (Scarpellini et al., 2014; Zhang et al., 2014), the chemical formula of which is $[M_{1-x}^{2+}M^{3+}(OH)_2]^{x+}(An^-)_{x/n}mH_2O$, in which the anion An^- is in the hydrated interlayer galleries (such as OH^-, NO_3^-, and PO_4^{3-}), and the metal cations M^{3+} and M^{2+} (such as Al^{3+}, Y^{3+}, and Mg^{2+}) occupy the octahedral holes in the brucite-like layer (Dong et al., 2014). This inorganic nanocontainer is widely applied in the research on corrosion protection because of high loadings, easy modification, and small size. Corrosion occurs when the corrosion environment destroys the main physical barrier of metals, causing the corrosive medium (such as Cl^-) to contact the bare metal substrate. Thus, the obvious feature of ion exchange is that it can release the interlayer anion and adsorb Cl^- when it confronts corrosive ions (Lu, 2018). As a result, the LDH film grown on the surface of anodized magnesium can not only seal the porous anodic oxide layer but also improve the thickness of the protective film successfully. Thus, this structure has a synergistic impact of promotion on improving the corrosion resistance of magnesium alloy.

As a unique two-dimensional-layered structure, the structure characteristics are maximized to the modification of LDHs to enhance the resistance of corrosion property. Nowadays, a great number of researchers (Zhang, 2017a; Zhang, 2017b; Zahedi Asl, 2019) paid more attention to change rare earth ions (La and Ce) in LDHs, and research studies started with being published in the study of corrosion. Zhou et al. (2019) found that the fabrication of ZnAlLa-LDHs can improve the anti-corrosion of 6,061 aluminum alloys. The phenomenon that MgAl-LDHs doping with Ce can enhance the corrosion protection property of magnesium alloys was found in one of our previous research studies (Zhang, 2018; Zahedi Asl, 2019; Zhang, 2019). However, compared to light rare earth elements (La, Ce), heavy rare earth elements (particularly Y) with low content on earth have no awareness. In addition, although Y has good corrosion inhibition performance, Y-doped ternary LDH films are rarely researched (He et al., 2010; Liu et al., 2010). In fact, ternary LDH has been widely studied in the field of catalysts. Y, La, and Ce addition in MgAl-LDHs can effectively enhance the performance of catalysis (Angelescu et al., 2004; Das et al., 2006; Mrózek, 2019) and luminescence activity (Smalenskaite et al., 2017). Particularly, compared with Ce and La, Y has the lowest electronegativity (1.22) and the smallest ionic radius (0.90 Å) in the same IIIB group (Wang et al., 2014), which makes it theoretically possible to carry Y in MgAl-LDH structure. Meanwhile, the adulteration of Y can improve the specific surface region (Świrk, 2019) and increase the dispersion of active sites (Pavel, 2011) as well as get finer LDH crystallites (Świrk, 2018), which can be used to make contributions to the synthesis of MgAlY-LDH film.

Moreover, the preparation of ternary LDHs usually uses the co-precipitation way. Recently, the study hotpot is that the *in situ* growth method is often used in preparing LDH film, which can contain less impurity phase concentration, possess the binding force between the substrate and film, and get a wide application prospect. Furthermore, the protective Y_2O_3 coating can be grown voluntarily on the surface of Mg substrates (Guo et al., 2010; Ardelean et al., 2013; Lyu et al., 2020). Furthermore, component cations can be provided by the anodic oxide film of Mg–2Zn–4Y alloys for *in situ* ternary LDHs, and the film can serve as a physical barrier to prevent the invasion of corrosive media. MgAlY-LDHs can possess the property of self-healing and anti-corrosion ability by the way of sealing the anodic oxide films (Bîrjega, 2005).

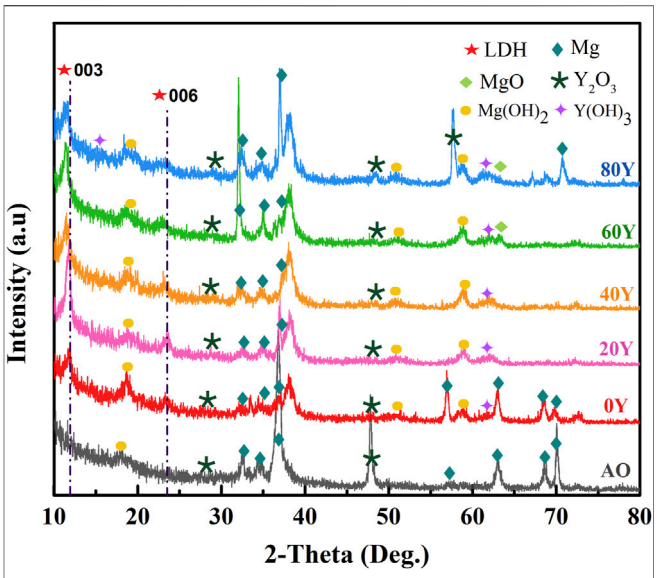

FIGURE 1 | XRD image of specimens with different Y% fabricated on anodized oxide films on Mg–2Zn–4Y alloys.

In this work, we investigated the possibility of ternary MgAlY-LDHs growing on the anodic oxide film of Mg–2Zn–4Y alloy *in situ* and investigated the isomorphous substitution mechanism of MgAlY-LDHs by adding different concentrations of Y. Furthermore, the morphology, structure characteristics, and composition of MgAlY-LDHs were studied. The corrosion resistance of MgAlY-LDHs was initially evaluated by electrochemical activity.

2 EXPERIMENTAL

2.1 Materials

Mg–2Zn–4Y alloy was manufactured in an anti-electric furnace under an environment of protective gas admixture (1% SF6 and 99% CO_2). The raw materials were commercially pure Mg (Ni % < 0.007%, Al % < 0.006%, Si % < 0.005%, Fe % < 0.004%, Cu % < 0.003%, and Mg ≥ 99.95%), pure Al (Al % ≥99.5%, impurity <0.15%), pure Zn (Ni % < 0.01%, Si % < 0.03%, Cu % < 0.01%, Al % < 0.03%, Fe % < 0.05%, and Zn % ≥ 99.9%), and Mg-Y master alloys (purity ≥99.5%, Ni% < 0.01%, Al % < 0.03%, Si % < 0.03%, Cu % < 0.01%, Fe % < 0.05%, and Y % = 30%). The alloys were melted at 750°C for 20 min, and then the film was placed in a mild steel mold (size φ200 mm × 85 mm) preheated at 300°C to

TABLE 1 | Structure data of specimens with different Y% fabricated on anodized oxide films on Mg–2Zn–4Y alloys.

Specimen	0Y	20Y	40Y	60Y	80Y	AO
Lattice constant a	3.0378	3.0466	3.0598	3.0456	3.0306	—
Lattice constant c	22.6353	22.6092	23.21295	23.1513	22.93815	—

(a) Lattice parameter a = 2 × d110, (b) c = 3/2(d003 + 2d006).

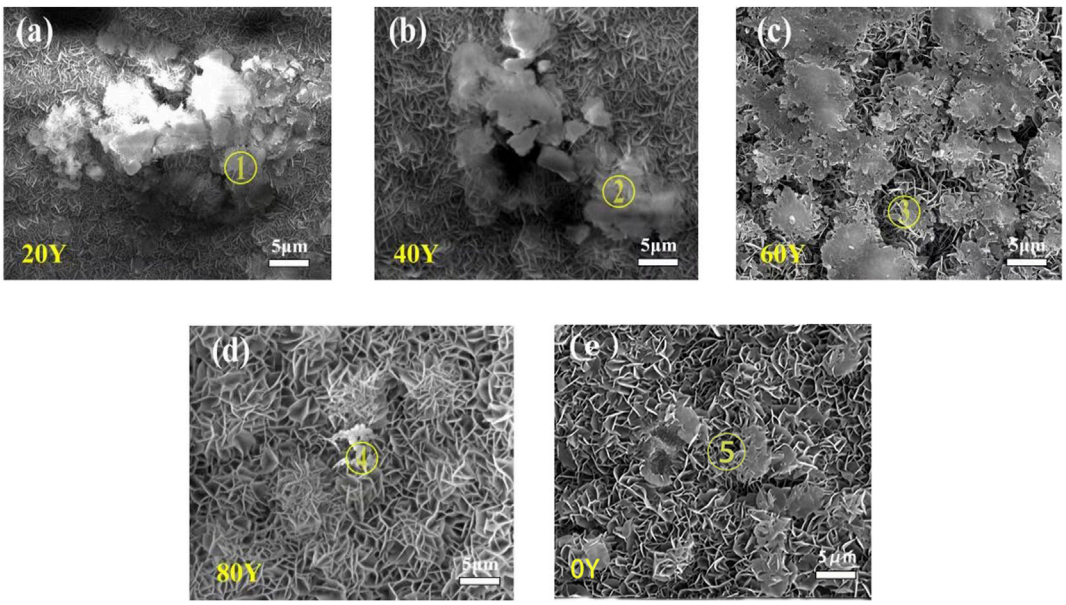

FIGURE 2 | SEM image of LDH specimens with different Y% fabricated on anodized oxide films on Mg–2Zn–4Y alloys: 20Y **(A)**; 40Y **(B)**; 60Y **(C)**; 80Y **(D)**; and 0Y **(E)**.

prepare Mg–2Zn–4Y ingots and finally cooled in an air solution for 6 h. The Mg–2Zn–4Y alloy was cut into slices of 10 mm × 10 mm × 2 mm and 20 mm × 20 mm × 2 mm. The samples were grounded from # 150 to # 3,000 using particle size silicon carbide sandpaper, washed with ethanol and deionized water, and finally dried.

2.2 Preparation of the Anodic Oxide Film

The samples were anodized in the successively stirred electrolyte of 0.6 mol/L NaF, 0.21 mol/L Na_3PO_4, and 3 mol/L NaOH, and the stable voltage is 20 V for 30 min by DC-regulated power. The prepared samples are anodic oxide films of the phosphoric acid system. All anodized samples are named AO. The cathode is made of 1Cr18Ni9Ti stainless steel, and the anode is made of magnesium alloy. The sample with the micro-arc oxidation film is cleaned with ethanol and dried.

2.3 Preparation of MgAlY-LDHs

The MgAlY-LDH films were produced by immersing the anodized samples in 0.3 M $NaNO_3$ and 0.05 M $M(NO_3)_3$ (M = Al and Y) mixture solution with a pH value in the alkaline range by putting the diluted ammonia on. The mixture solutions are put into the Teflon-lined autoclave, and the synthesis was performed at 125°C for 12 h. Then, the filmed samples were rinsed with deionized water, ultrasonically cleaned with ethanol, and finally dried under environmental conditions. Meanwhile, the *in situ* growth of MgAlY-LDH films on different anodic oxide films is researched by changing the ratio of Y^{3+} to Al^{3+} (including Al and Y ions): 0, 20, 40, 60, and 80%. The final samples prepared with different Y^{3+} concentrations are named as 0Y, 20Y, 40Y, 60Y, and 80Y.

2.3.1 Permission to Reuse and Copyright

Figures, tables, and images will be published under a Creative Commons CC-BY licence and permission must be obtained for use of copyrighted material from other sources (including re-published/adapted/modified/partial figures and images from the internet). It is the responsibility of the authors to acquire the licenses, to follow any citation instructions requested by third-party rights holders, and cover any supplementary charges.

2.4 Characterization and Performance Test

The morphology components of each sample are tested by VEGA3 field-emission scanning electron microscopy (FE-SEM, Vega3 TESCAN SRO Czech) and EDS. The crystal structure of ternary LDHs of each sample is examined using an X-ray

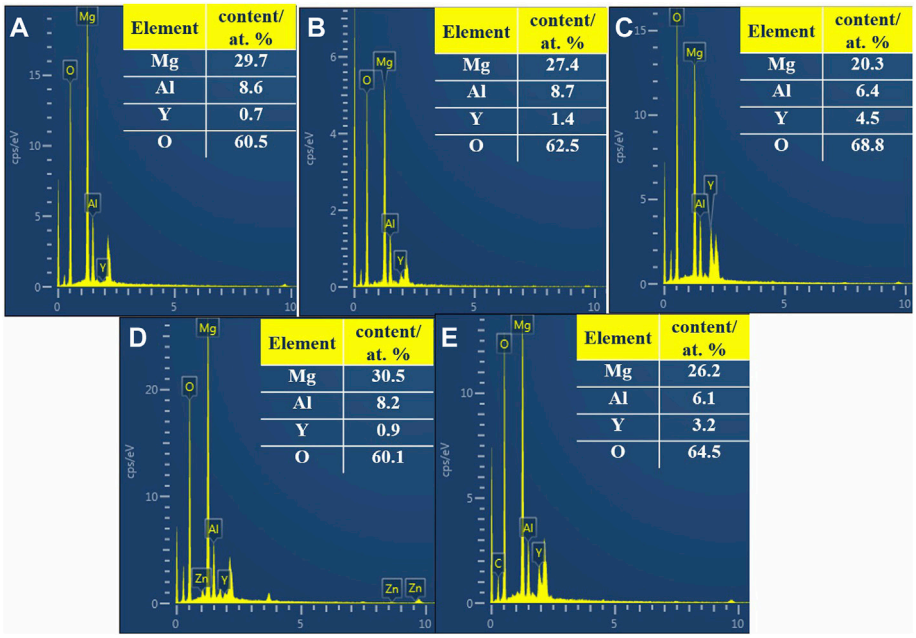

FIGURE 3 | EDS spectra of the corresponding points in **Figure 2**: 20Y [**(A)**, 1]; 40Y [**(B)**, 2]; 60Y [**(C)**, 3]; 80Y [**(D)**, 4]; and 0Y [**(E)**, 5].

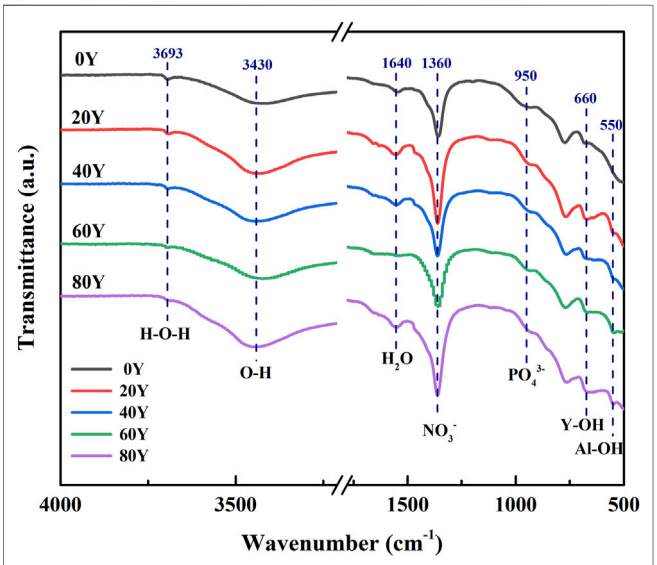

FIGURE 4 | FT-IR pattern of different specimens.

diffractometer (XRD, D/Max 2,500 × Rigaku Japan) and a Nicolet IS5 model Fourier infrared spectrometer (FT-IR, Nicolet IS5 Thermo Scientific, United States). The corrosion behavior of the sample in 3.5 wt% NaCl solution is tested using an electrochemical workstation (Parstat 4000A PAR, United States). A three-electrode battery system with the saturated calomel electrode as the reference electrode, the platinum mesh as the counter electrode, and the sample with an exposed area of 1 cm^2 as the working electrode is established in a Faraday electromagnetic shielding box. Among them, when the scan rate is set to 2 mV s^{-1}, the Tafel polarization curve with reference open circuit potential (OCP) from −0.8 to 0.8 V is obtained.

3 RESULTS AND DISCUSSION

3.1 Characterization of Film Composition, Structure, and Morphology

Figure 1 shows the XRD patterns of different specimens. Among all, the characteristic peaks of MgO and Y_2O_3 are found in all samples, which indicates the compound composition of the phosphate anodized film on Mg–2Zn–4Y alloy. Significantly, the characteristic peaks of Y_2O_3 and Mg substrate in samples 60Y and 80Y are more obvious than others. This may indicate that the moderate concentration of Y^{3+} is conducive to the dissolution of the anodized film. Furthermore, the characteristic peaks (003 and 006) are found in the each LDH sample. In particular, the peaks of 003 and 006 in 60Y shift most obviously to the left, that is to say, adulteration Y leads to the increase of the lattice parameter, interlayer distance, and crystallite dimension. This may indicate that the most obvious changes have taken place in the main structure of LDHs when Y^{3+}/Al^{3+} equals 1.5, which means *in situ* substitution is the strongest. In addition, the characteristic peaks of $Y(OH)_3$ are found in all samples. This may indicate that part of rare earth Y ions can turn to $Y(OH)_3$ on LDHs.

Table 1 illustrates the lattice parameters of specimens with different Y%, which can be calculated by the formula a, b inferred by XRD data. With the increasing proportion of Y, the lattice constants a and c are seen to increase in most specimens.

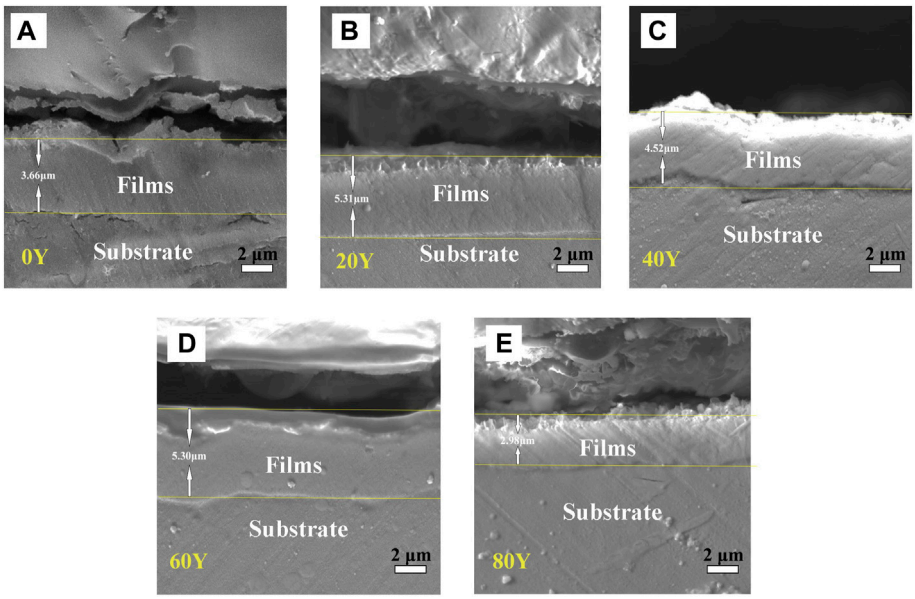

FIGURE 5 | Cross-sectional images of different specimens: 0Y **(A)**; 20Y **(B)**; 40Y **(C)**; 60Y **(D)**; and 80Y **(E)**.

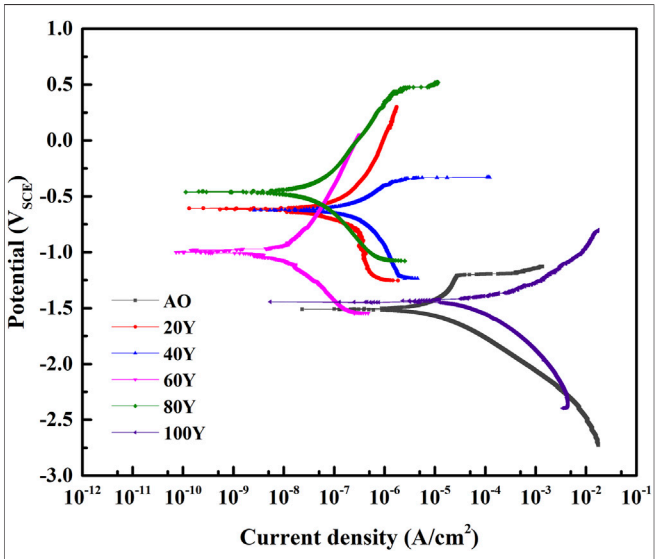

FIGURE 6 | Polarization curves of LDH specimens with different Y% fabricated on phosphoric acid anodized oxide films on Mg–2Zn–4Y alloys of specimens immersed in 3.5 wt% NaCl solution.

TABLE 2 | EDS profile recorded for the corresponding points on different specimens in **Figure 2**: 0Y (a, 1); 20Y (b, 2); 40Y (c, 3); 60Y (d, 4); and 80Y (e, 5).

Sample	0Y (at.%)	20Y (at.%)	40Y (at.%)	60Y (at.%)	80Y (at.%)
Mg	29.7	27.4	20.3	30.5	26.2
Al	8.6	8.7	6.4	8.2	6.1
Y	0.7	1.4	4.5	0.9	3.2
O	60.5	62.5	68.8	60.1	64.5

Generally, the lattice parameter-a is considered the interplanar distance, which equals the average distance of cations in LDH (Wang et al., 2019a). The slight increase of constant-a indicates that the large cations enter LDH, causing the planar distance enlarges, or even the fragmentation, and refinement resulting from the isovalent substitution. The big size of Y cations leads to the increase of planar distance abnormally. The prominent increase of parameter-c reveals the expansion of the interlayer passage (Wang et al., 2019a). The hydrated anion species significantly are relied on parameter-c, and the degree of trivalent cation substitution has an influence on electrostatic forces from anions (Smalenskaite et al., 2017; Wang et al., 2019b). Meanwhile, Y element has relatively low electronegativity, resulting in parameter-c increases by improving the electrostatic forces from anions. In addition, the parameter-a for 80 Y and parameter-c for 20Y show slight decline, which means Y species did not infiltrate LDH very well related to cracks between coatings and the substrate in **Figure 5**. The cracks cause volume expansion and irregular deformation, leading to constant a and c drops. Overall, the addition of Y species leads to obvious changes in structure data as shown in **Table 1**; **Figure 1**.

Figure 2 shows the SEM micrographs of samples. All the samples show typical undulating LDH nanosheet morphology, and some areas are covered with some substances (**Figures 2A–D**). **Figure 2** e shows that a great number of coarse lamellar structures are found. Moreover, EDS analysis of the protrusion area of the samples is shown in **Figure 3**; **Table 1**. The element contents of areas 1 and 2 in **Figure 2** show that the

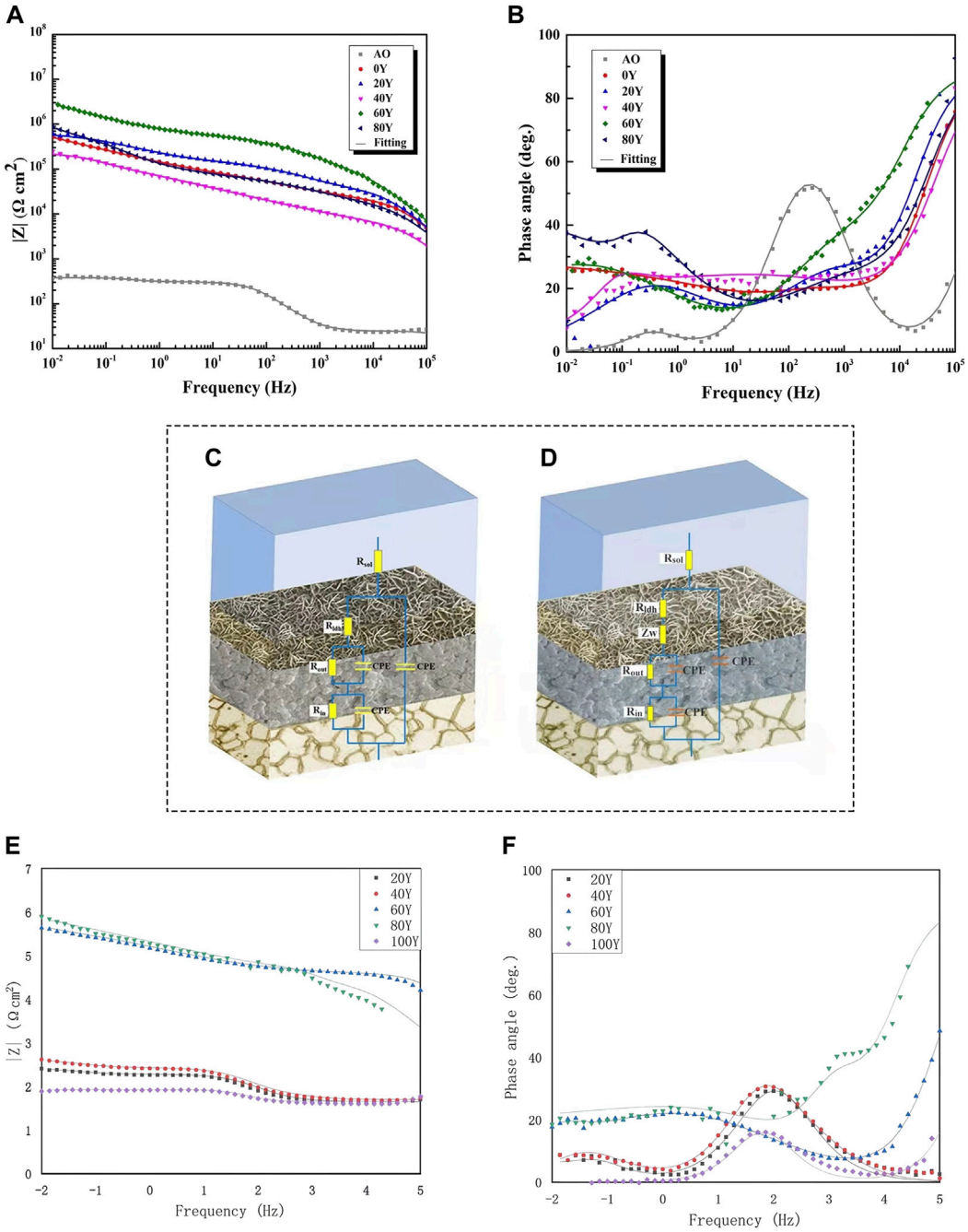

FIGURE 7 | EIS spectra of specimens immersed in 3.5 wt% NaCl solution. **(A,B)**; equivalent circuits and physical models of coatings **(C,D)**; EIS data and fitting curves (straight line) of different coatings in 3.5 wt% NaCl solution after immersion for **(E,F)** 4 days.

accumulated material may be $Y(OH)_3$. Area 3 shows a large number of clusters of LDHs distributed uniformly on the surface. The composition of ternary LDHs can be determined by EDS analysis. EDS analysis of some agglomerates in area 4 shows the morphology of incompletely crystallized ternary LDHs. The energy spectrum analysis of area 5 shows that the flake material may be Mg $(OH)_2$. Combining SEM and EDS analysis of different Y contents, the morphology of MgAlY-LDH nanosheets may be a convex cluster, and some rare earth Y ions in cluster-like material are covered on the LDH sheet. Some of the isomorphic substitutions of Al ions on Y ions existed, and ternary LDHs nanosheets were successfully obtained. In addition, rare earth ions (Y^{3+}), which are larger than aluminum ions, enter the LDH matrix layer to form a matrix crystal lattice, resulting in the morphology of ternary LDHs as convex clusters (Dai et al., 2021).

TABLE 3 | Fitted parameters of different specimens for the EIS spectrum.

Sample	R_s ($\Omega \cdot cm^2$)	CPE (S s^n cm^{-2})	N	R_{film} ($\Omega \cdot cm^2$)	W	CPE (S s^n cm^{-2})	n	R_{out} ($\Omega \cdot cm^2$)	CPE (S sn cm^{-2})	n	R_{in} ($k\Omega \cdot cm^2$	χ^2
AO	0.01	7.3×10^{-3}	1	7.1×10^4	—	1.5×10^{-5}	0.9	2.8×10^2	3.0×10^{-8}	1.0	2.4×10^0	5.3×10^{-3}
0Y	0.01	3.0×10^{-10}	1	1.6×10^4	—	4.7×10^{-6}	0.6	1.0×10^1	0.5×10^{-6}	0.8	1.9×10^1	1.6×10^{-3}
20Y	0.01	3.0×10^{-10}	1	3.0×10^4	—	1.4×10^{-7}	0.6	1.0×10^5	2.6×10^{-6}	0.6	5.2×10^5	1.2×10^{-3}
40Y	0.01	7.2×10^{-10}	1	1.9×10^4	—	7.5×10^{-7}	0.5	4.9×10^4	4.6×10^{-6}	0.5	4.9×10^4	6.6×10^{-3}
60Y	0.01	2.2×10^{-8}	1	7.9×10^4	—	3.3×10^{-8}	0.6	4.0×10^5	1.2×10^{-6}	0.4	1.2×10^7	1.9×10^{-3}
80Y	0.01	3.9×10^{-10}	1	1.3×10^4	5.5×10^{-6}	4.3×10^{-7}	0.5	5.3×10^4	1.3×10^{-5}	1.0	1.0×10^5	6.3×10^{-3}

TABLE 4 | Electrochemical parameters of different specimens.

Specimen	Ecorr (V SCE^{-1})	icorr (A cm^{-2})
AO20Y	–1.511–0.615	7.693 × 10–69.160 × 10–8
40Y	–0.761	1.080 × 10–7
60Y	–0.997	9.052 × 10–9
80Y	–0.459	2.933 × 10–8
0Y	–1.454	4.219 × 10–5

The FT-IR spectrum of each sample is shown in **Figure 4**. In the chemical formula of LDH, anions An^- contain OH^-, NO_3^- and PO_4^{3-}, and metal cations M^{3+} are composed of Al^{3+} and Y^{3+}. Meanwhile, the mental ion Y^{3+} is considered to relate to $Y(OH)_3$ in the XRD image (**Figure 1**.). Thus, the result of the FT-IR spectrum is in accordance with the XRD image. The vibration wavelengths of all samples at 3,693, 3,430, and 1,640 cm^{-1} correspond to the hydroxyl bands of water or LDHs, respectively (Luo, 2019). Each sample showed characteristic peaks at 1,360 and 950 cm^{-1}, which was attributed to the vibration absorption of NO_3^- and PO_4^{3-}, indicating the presence of NO_3^- and PO_4^{3-} in the interlayer of LDHs (Zăvoianu, 2018). In addition, the vibrational stretching of Y-OH appears in the band around 660cm^{-1}. In addition, the bands around 660 and 550 cm^{-1} are attributed to the vibrational stretching of Y-OH and Al-OH, respectively (Zhang, 2016; Zhang, 2019; Jiang et al., 2021). With the gradually increasing Y content, we can find that the strength of Y-OH increases gradually, indicating that more $Y(OH)_3$ is attached to the surface of the film.

The SEM image of the cross section of each sample is shown in **Figure 5**. The thickness of the samples of 0Y, 20Y, 40Y, 60Y, and 80Y correspond to 3.66, 5.31, 4.52, 5.30, and 2.98 μm, respectively. The reason why the thickness of the samples is different is that the growth condition of films is controlled by the concentration of Y. It can be seen from the cross-sectional image that the samples of 20Y, 40Y, and 60Y have grown a relatively thick film, which may indicate that 20Y, 40Y, and 60Y samples have appropriate conditions for film growth. However, there are cracks between the 0Y, 20Y, 40Y, and 80Y coatings and the substrate, indicating that the bonding force between the coating and the substrate is relatively poor. In addition, the cross section of the 60Y sample is relatively dense and thick, and there is no gap between the sample and the substrate, indicating that the coating has a better growth condition when the concentration is 60Y.

3.2 Corrosion Resistance Test of the Film

We make the corrosion resistance tests aiming at LDH specimens with different Y% fabricated on phosphoric acid anodized oxide films on Mg–2Zn–4Y alloys of specimens. **Figure 6** shows the polarization curves of different samples immersed in 3.5 wt% NaCl solutions. The electrochemical parameters corresponding to each polarization curve are listed in **Table 2**. Here, the corrosion potential (Ecorr) cannot measure the corrosion resistance of the coating because Ecorr will be significantly affected by thermodynamic properties of the material (Adsul et al., 2021; Cui et al., 2021). Usually, a lower corrosion density (icorr) is regarded as an excellent corrosion prevention property (Ramezanzadeh et al., 2016; Chen et al., 2022). It can be seen in **Table 2** that the current density of 20Y, 40Y, 60Y, and 80Y is close; among these, 20Y, 40Y, and 60Y have relatively thick coating making their current density rather low. However, it may indicate that because there are cracks between coating and substrate and the bonding force is poor in 20Y and 40Y, their current density is higher than 60Y, while 80Y has relatively thin coating leading to climbing of current density. Meanwhile, the 0Y and 100Y samples have more cracks and thin-film leading to corrosion current much higher than other samples. The 60Y sample has the lowest corrosion current, reaching 2.933×10^{-8} A cm^{-2}, indicating that the ternary MgAlY-LDH film prepared on the phosphoric acid anodic oxide film has the best corrosion resistance. Also, other samples with a concentration close to 60Y (20Y, 40Y, and 80Y) all have good corrosion resistance. Therefore, the LDH film grown *in situ* on the phosphoric acid anodic oxidation system has better corrosion resistance.

In order to study the corrosion resistance mechanism of different samples in a corrosive environment, electrochemical impedance spectroscopy was studied. The Bode impedance and phase angle spectra of different samples in 3.5 wt% NaCl solution are shown in **Figures 7A,B**. The impedance of matrix and coating is illustrated by the $|Z|_{0.01\ Hz}$ impedance. The high-frequency range reflects the properties of the coating (10^2–10^5 Hz), the middle frequency range reflects the inner layer (1–10^2 Hz), and the characteristics of the substrate and coating intersection are reflected in the low frequency (less than 1 Hz). The greater the value of the impedance modulus (*0.01 Hz*) in the low-frequency region, the better the corrosion resistance of the sample in a corrosive environment (Chen et al., 2020; Zhang et al., 2018; Chen et al., 2021). Among them, the 60Y sample has the highest impedance modulus of all samples, exceeding 10^6 Ω cm^2, which is an order of magnitude higher than the impedance value of the

anodized sample (**Figure 7A**). In the Bode-phase angle spectrum, three relaxation phenomena corresponding to the time constant can be found in all samples (**Figure 7B**). The time constant is used to characterize the structural characteristics and corrosion performance of the composite coating. **Table 3** has listed the fitted electrochemical impedance spectroscopy parameters. R_s is considered the electrolyte resistance. R_{film} corresponds to the sample surface film (LDHs) resistance. R_{out} *and* R_{in} represent the external porous layer resistance of the anodic oxide film and the internal dense layer resistance of the anodic oxide film, respectively. A larger R-value represents a better corrosion resistance of the coating. The constant phase element (CPE) is the response capacitance connected in parallel with the corresponding resistance. n indicates the angular frequency, and it can be considered that CPE is an ideal capacitor when n is close to 1. The lower the chi-squared error (χ^2) indicates that the circuit fits well (Cui et al., 2018; Chen, 2019). At low frequency, diffusion of the corrosion medium affects the control corrosion process (Ye, 2018). Therefore, a Warburg impedance part (Z_W) is included in the circuit of the 80Y specimen. SEM and EDS show that (**Figure 2** and **Figure 3**) a passivation film of Y $(OH)_3$ is formed on the coating surface when the content of Y is relatively high, and it has a certain protective effect on the sample (Ye, 2018). Compared with other coatings, the values of R_{film}, $R_{out,}$ and R_{in} of the 60Y sample are the largest among all the tests, and the corrosion resistance is the highest, indicating that the ternary MgAlY-LDHs formed by the 60Y sample has the best corrosion performance (**Table 4**).

Figure 7 (e.f.) illustrates the Bode impedance plots of the different coatings during the 4 days. After 4 days of immersion, 60Y still has the largest |Z| 0.01 Hz value, which indicates that 60Y has the best corrosion resistance. At intermediate frequency, the phase angles of 0Y, 20Y, 40Y, and 80Y decrease quickly, indicating that the electrolyte penetrates these samples' coating system. However, 60Y has an increasing phase angle, indicating that the electrochemical reaction does not occur under the coating. In conclusion, the coating of 60Y has the best performance in corrosion resistance.

4 CONCLUSION

The MgAlY-LDH film was fabricated successfully on the anodized film of Mg–2Zn–4Y alloys. The introduction of Y ions with larger ionic radius into the LDH laminates affects the crystal lattice changes of LDHs and ultimately leads to the formation of MgAlY-LDH nanosheets in the shape of convex clusters of flowers. MgAlY-LDHs can adsorb the corrosive medium (Cl^-) into the intermediate layer in a corrosive environment, thereby triggering the stable appearance of the Y element and improving the corrosion performance of LDHs.

DATA AVAILABILITY STATEMENT

The original contributions presented in the study are included in the article/Supplementary Material; further inquiries can be directed to the corresponding author.

AUTHOR CONTRIBUTIONS

YH: conceptualization, investigation, methodology, data curation, and writing—original draft. LW: conceptualization, methodology, supervision, writing—review and editing, and funding acquisition. XZ: writing—review and editing and investigation. GZ: methodology. YC: investigation. TW: formal analysis. XD: methodology. JX: investigation. YZ: formal analysis. FP: writing—review and editing.

FUNDING

This work was supported by the National Natural Science Foundation of China (51971040, 52171101), the Natural Science Foundation of Chongqing (cstc2021jcyj-msxmX0613), National College Students' Innovation and Entrepreneurship Training Program(202110611045), and the National Natural Science Foundation of China (52001036, 51971044).

ACKNOWLEDGMENTS

We thank the Analytical and Testing Center of Chongqing University for performing the SEM test and National Engineering Research Center for magnesium Alloys for XRD, FT-IR, and electrochemical experiments.

REFERENCES

Adsul, S. H., Bagale, U. D., Sonawane, S. H., and Subasri, R. (2021). Release Rate Kinetics of Corrosion Inhibitor Loaded Halloysite Nanotube-Based Anticorrosion Coatings on Magnesium Alloy AZ91D. *J. Magnesium Alloys* 9 (1), 202–215. doi:10.1016/j.jma.2020.06.010

Angelescu, E., Pavel, O. D., Che, M., Bîrjega, R., and Constentin, G. (2004). Cyanoethylation of Ethanol on Mg-Al Hydrotalcites Promoted by Y^{3+} and La^{3+}. *Catal. Commun.* 5 (10), 647–651. doi:10.1016/j.catcom.2004.07.016

Ardelean, H., Seyeux, A., Zanna, S., Prima, F., Frateur, I., and Marcus, P. (2013). Corrosion Processes of Mg-Y-Nd-Zr Alloys in Na_2SO_4 Electrolyte. *Corros. Sci.* 73, 196–207. doi:10.1016/j.corsci.2013.03.036

Atrens, A. (2015). Review of Recent Developments in the Field of Magnesium Corrosion: Recent Developments in Mg Corrosion. *Adv. Eng. Mater.* 17, 2–3. doi:10.1002/adem.201400434

Bîrjega, R. (2005). Rare-earth Elements Modified Hydrotalcites and Corresponding Mesoporous Mixed Oxides as Basic Solid Catalysts. *Appl. Catal. A General* 288 (1), 185–193. doi:10.1016/j.apcata.2005.04.030

Blawert, C., Dietzel, W., Ghali, E., and Song, G. (2006). Anodizing Treatments for Magnesium Alloys and Their Effect on Corrosion Resistance in Various Environments. *Adv. Eng. Mater.* 8, 511–533. doi:10.1002/adem.200500257

Chen, Y. (2019). Enhanced Corrosion Protective Performance of Graphene Oxide-Based Composite Films on AZ31 Magnesium Alloys in 3.5 Wt% NaCl Solution. *Appl. Surf. Sci.* 493, 1224–1235.

Chen, Y., Ren, B., Gao, S., and Cao, R. (2020). The Sandwich-like Structures of Polydopamine and 8-Hydroxyquinoline Coated Graphene Oxide for Excellent Corrosion Resistance of Epoxy Coatings. *J. Colloid Interface Sci.* 565, 436–448. doi:10.1016/j.jcis.2020.01.051

Chen, Y., Wu, L., Yao, W., Chen, Y., Zhong, Z., Ci, W., et al. (2022). A Self-Healing Corrosion Protection Coating with Graphene Oxide Carrying 8-Hydroxyquinoline Doped in Layered Double Hydroxide on a Micro-arc Oxidation Coating. *Corros. Sci.* 194, 109941. doi:10.1016/j.corsci.2021.109941

Chen, Y., Wu, L., Yao, W., Zhong, Z., Chen, Y., Wu, J., et al. (2021). One-step *In Situ* Synthesis of Graphene Oxide/MgAl-Layered Double Hydroxide Coating on a Micro-arc Oxidation Coating for Enhanced Corrosion Protection of Magnesium Alloys. *Surf. Coatings Technol.* 413, 127083. doi:10.1016/j.surfcoat.2021.127083

Cui, L.-Y., Gao, L., Zhang, J.-C., Tang, Z., Fan, X.-L., Liu, J.-C., et al. (2021). *In Vitro* corrosion Resistance, Antibacterial Activity and Cytocompatibility of a Layer-By-Layer Assembled DNA Coating on Magnesium Alloy. *J. Magnesium Alloys* 9 (1), 266–280. doi:10.1016/j.jma.2020.03.009

Cui, M., Ren, S., Zhao, H., Xue, Q., and Wang, L. (2018). Polydopamine Coated Graphene Oxide for Anticorrosive Reinforcement of Water-Borne Epoxy Coating. *Chem. Eng. J.* 335, 255–266. doi:10.1016/j.cej.2017.10.172

Dai, X., Wu, L., Xia, Y., Chen, Y., Zhang, Y., Jiang, B., et al. (2021). Intercalation of Y in Mg-Al Layered Double Hydroxide Films on Anodized AZ31 and Mg-Y Alloys to Influence Corrosion Protective Performance. *Appl. Surf. Sci.* 551, 149432. doi:10.1016/j.apsusc.2021.149432

Das, J., Das, D., and Parida, K. M. (2006). Preparation and Characterization of Mg-Al Hydrotalcite-Like Compounds Containing Cerium. *J. Colloid Interface Sci.* 301 (2), 569–574. doi:10.1016/j.jcis.2006.05.014

Dong, Y., Wang, F., and Zhou, Q. (2014). Protective Behaviors of 2-Mercaptobenzothiazole Intercalated Zn-Al-Layered Double Hydroxide Coating. *J. Coat. Technol. Res.* 11 (5), 793–803. doi:10.1007/s11998-014-9568-9

Guo, X., Zhang, F., Evans, D. G., and Duan, X. (2010). Layered Double Hydroxide Films: Synthesis, Properties and Applications. *Chem. Commun. Camb. Engl.* 46, 5197–5210. doi:10.1039/c0cc00313a

He, W., Zhang, E., and Yang, K. (2010). Effect of Y on the Bio-Corrosion Behavior of Extruded Mg-Zn-Mn Alloy in Hank's Solution. *Mater. Sci. Eng. C* 30, 167–174. doi:10.1016/j.msec.2009.09.014

Hornberger, H., Virtanen, S., and Boccaccini, A. R. (2012). Biomedical Coatings on Magnesium Alloys - A Review. *Acta biomater.* 8, 2442–2455. doi:10.1016/j.actbio.2012.04.012

Huang, Y., Jin, F.-M., Chen, F.-J., and Chen, L. (2014). Improved Cycle Stability and High-Rate Capability of Li_3VO_4-Coated $Li[Ni_{0.5}Co_{0.2}Mn_{0.3}]O_2$ Cathode Material Under Different Voltages. *J. Power Sources* 256, 1–7. doi:10.1016/j.jpowsour.2014.01.003

Jiang, Q., Lu, D., Wang, N., Wang, X., Zhang, J., Duan, J., et al. (2021). The Corrosion Behavior of Mg-Nd Binary Alloys in the Harsh Marine Environment. *J. Magnesium Alloys* 9 (1), 292–304. doi:10.1016/j.jma.2019.12.010

Liu, M., Schmutz, P., Uggowitzer, P. J., Song, G., and Atrens, A. (2010). The Influence of Yttrium (Y) on the Corrosion of Mg-Y Binary Alloys. *Corros. Sci.* 52 (11), 3687–3701. doi:10.1016/j.corsci.2010.07.019

Lu, H. (2018). Comparative Study on Synchronous Adsorption of Arsenate and Fluoride in Aqueous Solution onto MgAlFe-LDHs with Different Intercalating Anions. *RSC Adv.* 8, 33301–33313.

Luo, S. (2019). Synthesis of Calcined La-Doped Layered Double Hydroxides and Application on Simultaneously Removal of Arsenate and Fluoride. *J. Solid State Chem.* 275, 275. doi:10.1016/j.jssc.2019.04.017

Lyu, J., Kim, J., Liao, H., She, J., Song, J., Peng, J., et al. (2020). Effect of Substitution of Zn with Ni on Microstructure Evolution and Mechanical Properties of LPSO Dominant Mg-Y-Zn Alloys. *Mater. Sci. Eng. A* 773, 138735. doi:10.1016/j.msea.2019.138735

Mordike, B. L., and Ebert, T. (2001). Magnesium. *Mater. Sci. Eng. A* 302 (1), 37–45. doi:10.1016/s0921-5093(00)01351-4

Mrózek, O. (2019). Mg-Al-La LDH-$MnFe_2O_4$ Hybrid Material for Facile Removal of Anionic Dyes from Aqueous Solutions. *Appl. Clay Sci.* 169, 1–9.

Pavel, O. D. (2011). The Activity of Yttrium-Modified Mg,Al Hydrotalcites in the Epoxidation of Styrene with Hydrogen Peroxide. *Appl. Catal. A General* 403 (1), 83–90. doi:10.1016/j.apcata.2011.06.017

Polmear, I. (2017). *Light Alloys : Metallurgy of the Light Metals*. Butterwort: Elsevier.

Prado, M. T. P., and Cepeda-Jiménez, C. M. (2015). Strength Ceiling Smashed for Light Metals. *Nature* 528, 486–487. doi:10.1038/528486a

Ramezanzadeh, B., Ahmadi, A., and Mahdavian, M. (2016). Enhancement of the Corrosion Protection Performance and Cathodic Delamination Resistance of Epoxy Coating through Treatment of Steel Substrate by a Novel Nanometric Sol-Gel Based Silane Composite Film Filled with Functionalized Graphene Oxide Nanosheets. *Corros. Sci.* 109, 182–205. doi:10.1016/j.corsci.2016.04.004

Scarpellini, D., Falconi, C., Gaudio, P., Mattoccia, A., Medaglia, P. G., Orsini, A., et al. (2014). Morphology of Zn/Al Layered Double Hydroxide Nanosheets Grown onto Aluminum Thin Films. *Microelectron. Eng.* 126, 129–133. doi:10.1016/j.mee.2014.07.007

Smalenskaite, A., Vieira, D. E. L., Salak, A. N., Ferreira, M. G. S., Katelnikovas, A., and Kareiva, A. (2017). A Comparative Study of Co-precipitation and Sol-Gel Synthetic Approaches to Fabricate Cerium-Substituted Mg Al Layered Double Hydroxides with Luminescence Properties. *Appl. Clay Sci.* 143, 175–183. doi:10.1016/j.clay.2017.03.036

Srinivas, A., Pavan, D., Venkatesha, B. K., Rao, R. R., and Mohith, L. (2022). Study on Mechanical Properties of AZ91 Magnesium Alloy. *Mater. Today Proc.* 54, 291–294. doi:10.1016/j.matpr.2021.09.171

Stoltenhoff, T., Kreye, H., and Richter, H. J. (2002). An Analysis of the Cold Spray Process and its Coatings. *J. Therm. Spray Technol.* 11, 542–550. doi:10.1361/105996302770348682

Świrk, K. (2018). Yttrium Promoted Ni-Based Double-Layered Hydroxides for Dry Methane Reforming. *J. CO2 Util.* 27, 247–258.

Świrk, K. (2019). Ce- and Y-Modified Double-Layered Hydroxides as Catalysts for Dry Reforming of Methane: On the Effect of Yttrium Promotion. *Catalysts* 9, 56.

Wang, J., Wei, F., Shi, B., Ding, Y., and Jin, P. (2019a). The Effect of Y Content on Microstructure and Tensile Properties of the As-Extruded Mg-1Al-xY Alloy. *Mater. Sci. Eng. A* 765, 138288. doi:10.1016/j.msea.2019.138288

Wang, Y., Zhang, Y., Zhou, B., Li, C., Gao, F., Wang, X., et al. (2019b). *In-situ* Observation of the Growth Behavior of ZnAl Layered Double Hydroxide Film Using EQCM. *Mater. Des.* 180, 107952. doi:10.1016/j.matdes.2019.107952

Wang, Z., Fongarland, P., Lu, G., and Essayem, N. (2014). Reconstructed La-, Y-, Ce-Modified MgAl-Hydrotalcite as a Solid Base Catalyst for Aldol Condensation: Investigation of Water Tolerance. *J. Catal.* 318, 108–118. doi:10.1016/j.jcat.2014.07.006

Ye, Y. (2018). One-step Synthesis of Superhydrophobic Polyhedral Oligomeric Silsesquioxane-Graphene Oxide and its Application in Anti-corrosion and Anti-Wear Fields. *Corros. Sci.* 147, 9. doi:10.1016/j.corsci.2018.10.034

Zahedi Asl, V. (2019). The Effect of Cerium Cation on the Microstructure and Anti-Corrosion Performance of LDH Conversion Coatings on AZ31 Magnesium Alloy. *J. Alloys Compd.* 821, 153248.

Zăvoianu, R. (2018). Effect of Hydration Temperature on the Structure Reconstruction of MgAlY Layered Materials. *Comptes Rendus Chim.* 21 (3), 318–326.

Zhang, F. (2016). Corrosion Resistance of the Superhydrophobic Mg(OH)2/Mg-Al Layered Double Hydroxide Coatings on Magnesium Alloys. *Metals* 6 (4), 85. doi:10.3390/met6040085

Zhang, F., Liu, Z.-G., Zeng, R.-C., Li, S.-Q., Cui, H.-Z., Song, L., et al. (2014). Corrosion Resistance of Mg-Al-LDH Coating on Magnesium Alloy AZ31. *Surf. Coatings Technol.* 258, 1152–1158. doi:10.1016/j.surfcoat.2014.07.017

Zhang, G. (2018). Active Corrosion Protection by a Smart Coating Based on a MgAl-Layered Double Hydroxide on a Cerium-Modified Plasma Electrolytic Oxidation Coating on Mg Alloy AZ31. *Corros. Sci.* 139, 370. doi:10.1016/j.corsci.2018.05.010

Zhang, G. (2019). *In-situ* Grown Super- or Hydrophobic Mg-Al Layered Double Hydroxides Films on the Anodized Magnesium Alloy to Improve Corrosion Properties. *Surf. Coatings Technol.*, 366. doi:10.1016/j.surfcoat.2019.03.016

Zhang, G., Wu, L., Tang, A., Pan, H., Ma, Y., Zhan, Q., et al. (2018). Effect of Micro-arc Oxidation Coatings Formed at Different Voltages on the *In Situ* Growth of Layered Double Hydroxides and Their Corrosion Protection. *J. Electrochem. Soc.* 165 (7), C317–C327. doi:10.1149/2.0531807jes

Zhang, Y. (2017a). Double-doped LDH Films on Aluminum Alloys for Active Protection. *Mater. Lett.*, 192. doi:10.1016/j.matlet.2017.01.038

Zhang, Y. (2017b). Enhancement of Anticorrosion Protection via Inhibitor-Loaded ZnAlCe-LDH Nanocontainers Embedded in Sol–Gel Coatings. *J. Coatings Technol. Res.* 15, 1–11. doi:10.1007/s11998-017-9978-6

Zhou, B., Wei, X., Wang, Y., Huang, Q., Hong, B., and Wei, Y. (2019). Effect of Lanthanum Addition on Microstructures and Corrosion Behavior of ZnAl-LDHs Film of 6061 Aluminum Alloys. *Surf. Coatings Technol.* 379, 125056. doi:10.1016/j.surfcoat.2019.125056

Conflict of Interest: The authors declare that the research was conducted in the absence of any commercial or financial relationships that could be construed as a potential conflict of interest.

Publisher's Note: All claims expressed in this article are solely those of the authors and do not necessarily represent those of their affiliated organizations, or those of the publisher, the editors and the reviewers. Any product that may be evaluated in this article, or claim that may be made by its manufacturer, is not guaranteed or endorsed by the publisher.

Copyright © 2022 Hong, Wu, Zhang, Zhan, Chen, Yao, Dai, Wu, Dai, Xiang, Zhou and Pan. This is an open-access article distributed under the terms of the Creative Commons Attribution License (CC BY). The use, distribution or reproduction in other forums is permitted, provided the original author(s) and the copyright owner(s) are credited and that the original publication in this journal is cited, in accordance with accepted academic practice. No use, distribution or reproduction is permitted which does not comply with these terms.